Small

NANO · MICRO small
www.small-journal.com

RESEARCH ARTICLE OPEN ACCESS

Water Droplet Hammer: Piezoelectric Sensing of Ultrafast Mechanical Transients During Droplet Impact

Ian Kim[1] | Chen Lin[1] | Zuer Wu[1] | Siyuan Rao[1,2] | Qianbin Wang[1]

[1]Department of Biomedical Engineering, Binghamton University, State University of New York, Binghamton, New York, USA | [2]Integrative Neuroscience Program, Binghamton University, State University of New York, Binghamton, New York, USA

Correspondence: Siyuan Rao (syrao@binghamton.edu) | Qianbin Wang (qbwang@binghamton.edu)

Received: 23 March 2026 | **Revised:** 25 June 2026 | **Accepted:** 2 July 2026

Keywords: droplet impact | interfacial oscillation | PVDF piezoelectric sensing | substrate-coupled strain | superhydrophobic surface

ABSTRACT

Erosion and fracture caused by repeated water-droplet impacts are often attributed to splash-mediated material removal, high-pressure impulsive loading, or cavitation. Yet, the mechanical response during the earliest instant of impact remains difficult to capture. Using a high-temporal-resolution polyvinylidene fluoride (PVDF) piezoelectric sensor combined with high-speed imaging, we directly measure substrate-coupled mechanical transients during a single water-droplet impact. A strong impulsive strain response appears within the first 2 ms after contact, followed by coherent 100–500 Hz oscillations at the water–solid interface during the first 20 ms, before any rebound occurs. The oscillation frequency is modulated by an effective interfacial stiffness, whereas the impulsive peak-to-peak response scales with droplet size and impact velocity. The experimentally captured signals provide direct experimental evidence of ultrafast substrate-coupled mechanical transients during droplet impact and establish a minimal inertial-capillary framework for understanding mechanical signatures that may contribute to low- to moderate-speed droplet-induced erosion and fatigue.

1 | Introduction

Droplet impacts have long been recognized as a source of material erosion and fracture [1–3]. The idea that persistent water droplets can wear down even the hardest surfaces appears in cultural observations dating back thousands of years, including the ancient Chinese proverb "drops of water wear holes in stone" and Ovid's remark that "dripping water hollows out stone" (Figure 1A). Modern studies typically attribute droplet-induced erosion to splash erosion, high-pressure impulsive loading, or cavitation, yet the mechanical events occurring at the moment of impact remain incompletely resolved [4–6].

When a liquid droplet impacts a solid surface, high-speed imaging reveals rapid deformation, spreading, and either rebound or deposition on timescales of several to tens of milliseconds [5, 7–11]. Imaging from a high-speed camera provides rich morphological information from multiple viewing angles [12, 13], but it does not directly measure substrate loading, and it lacks an intrinsic temporal reference for interfacial stress [14, 15]. Manual synchronization based on frame rate limits the ability to resolve microsecond-to-millisecond mechanical transients. Direct force measurements have revealed a secondary force spike during water droplet impact on superhydrophobic surfaces before rebound [16–18], indicating complex early-stage dynamics, but

Ian Kim and Chen Lin contributed equally to this work.

This is an open access article under the terms of the Creative Commons Attribution-NonCommercial License, which permits use, distribution and reproduction in any medium, provided the original work is properly cited and is not used for commercial purposes.
© 2026 The Author(s). *Small* published by Wiley-VCH GmbH

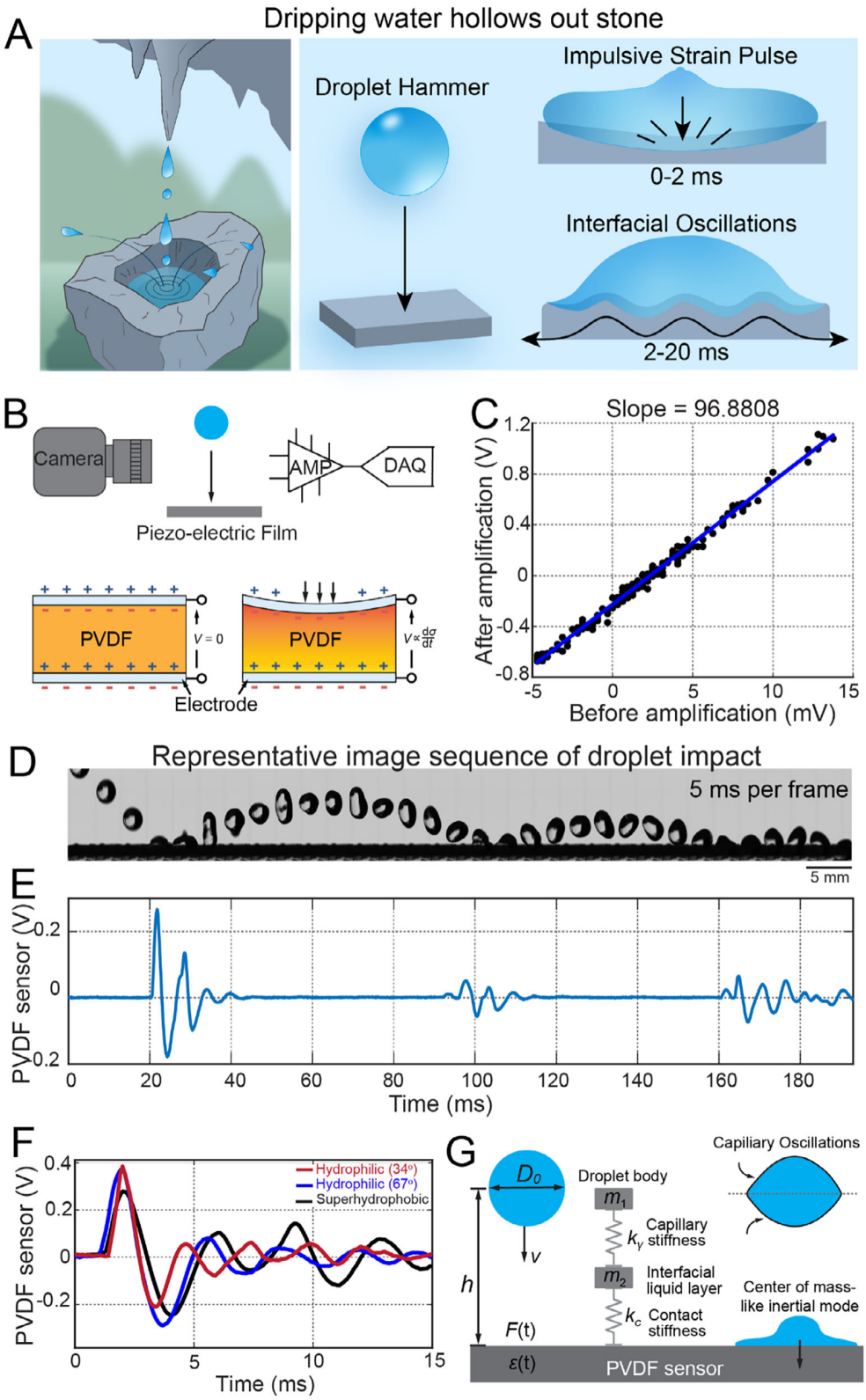

FIGURE 1 | PVDF-based measurement of droplet-impact dynamics. (A) Schematic of the "dripping water hollows out stone" mechanism, highlighting an initial impulsive strain pulse followed by interfacial oscillations before rebound. (B) PVDF strain-sensing platform integrated with a custom amplifier, DAQ system, and combined high-speed imaging. AMP: amplifier; DAQ: data acquisition. (C) Calibration of PVDF signals before and after amplification, showing an effective gain of 96.9×. (D, E) Representative high-speed image sequence (D) and corresponding PVDF strain waveform (E) during droplet impact on a superhydrophobic surface. (F) Droplet-impact dynamics on surfaces with different contact angles. (G) Minimal two-degree-of-freedom mass–spring–damper model describing substrate-coupled droplet-impact response.

16136829, 2026, 0, Downloaded from https://onlinelibrary.wiley.com/doi/10.1002/smll.74628. By Wiley Online Library, Wiley Online Library on [19/08/2026]. See the Terms and Conditions (https://onlinelibrary.wiley.com/terms-and-conditions) on Wiley Online Library for rules of use; OA articles are governed by the applicable Creative Commons License

the detailed temporal structure of this loading has not been directly resolved.

2 | Results

2.1 | Piezoelectric Sensing Reveals a Two-Stage Substrate-Coupled Response to Droplet Impact

We developed a high temporal resolution strain-sensing platform based on a PVDF piezoelectric film coupled to a custom amplifier to directly measure substrate-coupled mechanical signals during droplet impact (Figure 1B). Because PVDF functions as a dynamic piezoelectric sensor, the measured voltage reflects the time-dependent deformation of the coupled sensor–substrate system and is inherently sensitive to the rate of mechanical loading. Under fixed sensor geometry, substrate configuration, and amplifier gain, the peak-to-peak PVDF sensor signal is therefore interpreted as a relative measure of transient, impact-induced loading, rather than an absolute or statically calibrated force. The sensor is bonded to a glass substrate and read out by a charge amplifier and is integrated with a high-speed camera that captures the droplet morphology. Typical droplet impacts exert forces on the order of millinewtons and even micronewtons during rebound [19, 20]. To resolve the associated small signals, we implemented a 100× amplifier, achieving an effective gain of 96.9 as verified by comparing raw and amplified signals (Figure 1C and Figure S1).

For a representative water droplet of radius ~1 mm ($\gamma = 0.072$ N/m) impacting a superhydrophobic surface with a contact angle of 154.0°, the complete impact and rebound sequence is captured in both the high-speed camera images and the PVDF sensor's signal (Figure 1D,E, and Figure S2). The image sequence identifies the major morphological events, including initial contact, spreading, recoiling, and rebound, whereas the PVDF sensor's signal resolves the corresponding substrate-coupled mechanical response with higher temporal resolution. During each millisecond-scale contact event, including rebounds at approximately 21.8, 97.7, and 164.7 ms, the PVDF sensor's signal consistently exhibits a similar 100–500 Hz oscillatory structure (Figure 1E and Figure S3). The initial impact, occurring between 20 and 40 ms in the PVDF sensor readout, exhibits a clear two-stage signature: a strong, short-duration impulsive PVDF sensor response within the first 1–2 ms after contact, followed by a sequence of damped oscillatory waves.

To probe the role of surface wettability, we prepared substrates with different equilibrium contact angles: glass coated with polyvinyl alcohol (PVA, contact angle 34.4° ± 4.4°), bare glass (67.4° ± 12.7°), and glass coated with hydrophobically modified nanoparticles (NPs) to produce a superhydrophobic surface (154.0° ± 3.2°). For all three cases, the PVDF sensor readout shows the same qualitative temporal sequence: an intense impulsive strain pulse followed by coherent oscillations in the first 15 ms before rebound (Figure 1F). Both the half-period of the impulsive response and the oscillation period decrease monotonically as the surface changes from superhydrophobic to more hydrophilic.

The observed waveform suggests that the droplet-substrate system can be interpreted as a coupled inertial interfacial oscillator. Building on classic inertio-capillary theory and the Rayleigh frequencies of droplet oscillations [21–24], we describe the interaction using a minimal two-degree-of-freedom mass-spring-damper system (Figure 1G). This reduced-order model is not intended to replace the full hydrodynamic description of droplet spreading or contact-line motion, but rather to capture the dominant substrate-coupled temporal features measured by the PVDF sensor during the earliest stage of impact. A lower spring-mass element represents the interfacial liquid layer that deforms together with the substrate and is characterized by an effective contact stiffness k_c. An upper mass m_1 represents the remaining portion of the droplet that retains downward inertia after impact and is connected to the interfacial layer by a capillary spring of stiffness k_γ that captures the restoring action of surface tension. Within this framework, a center of mass (COM) mode corresponds to the motion of m_1 against the combined stiffness $k_c + k_\gamma$. This mode generates a short, intense inertial hammer at first touchdown and sets the amplitude of the initial impulsive strain peak [18, 25, 26]. A second, capillary-mediated mode arises from relative motion between the interfacial region and the deforming free surface, with a characteristic timescale related to inertio-capillary droplet recovery and classical Rayleigh-type oscillations [21–23]. In the PVDF measurements, this coupled two-mode oscillator produces the coherent oscillations that follow the impulsive event and, on low-adhesion hydrophobic substrates, a secondary strain peak that reflects impact-driven deformation and recovery of the local droplet–substrate interface.

2.2 | Wettability Modulates Rebound Behavior and Early-Stage Oscillation Dynamics

To minimize chemical heterogeneity while tuning wettability, glass substrates were coated with polystyrene (PS) containing different volume fractions of 1H,1H,2H, and 2H perfluorooctyltrichlorosilane (PFOTS)-modified silicon dioxide (SiO_2) nanoparticles, which introduce controlled micro-and nanoscale roughness [27–29]. Scanning electron microscopy (SEM) confirms that surface roughness increases with nanoparticle loading (Figure 2A and Figure S4). Pure PS (0% NPs) yields a relatively smooth surface with a static contact angle of 100.4° ± 5.2°, while 10% (v/v) NPs raises the contact angle to 123.2° ± 9.3°. Increasing the NP fraction from 25% to 75% produces superhydrophobic surfaces with contact angles exceeding 150°, with no significant differences among these highly rough surfaces (Figure 2B).

High-speed imaging shows that droplets on high adhesion surfaces (0% and 10% NPs) pin and undergo damped oscillations without rebounding, whereas droplets on superhydrophobic, low adhesion surfaces (contact angle >150°) rebound robustly (Figure 2C), consistent with the simultaneous PVDF measurements (Figure S5A) and previous reports on bouncing and contact time on hydrophobic and superhydrophobic substrates [20, 30, 31]. The first rebound time increases systematically with NP concentration (Figure S5B), indicating that reduced droplet surface adhesion and drag promote faster recoiling and rebound. Although the adhesive forces are too small to measure reliably with standard microbalances for the 25%–75% NPs groups, the PVDF sensor resolves subtle differences in rebound dynamics through precise timing.

16136829, 2026, 0, Downloaded from https://onlinelibrary.wiley.com/doi/10.1002/smll.74628. By Wiley Online Library, Wiley Online Library on [19/08/2026]. See the Terms and Conditions (https://onlinelibrary.wiley.com/terms-and-conditions) on Wiley Online Library for rules of use; OA articles are governed by the applicable Creative Commons License

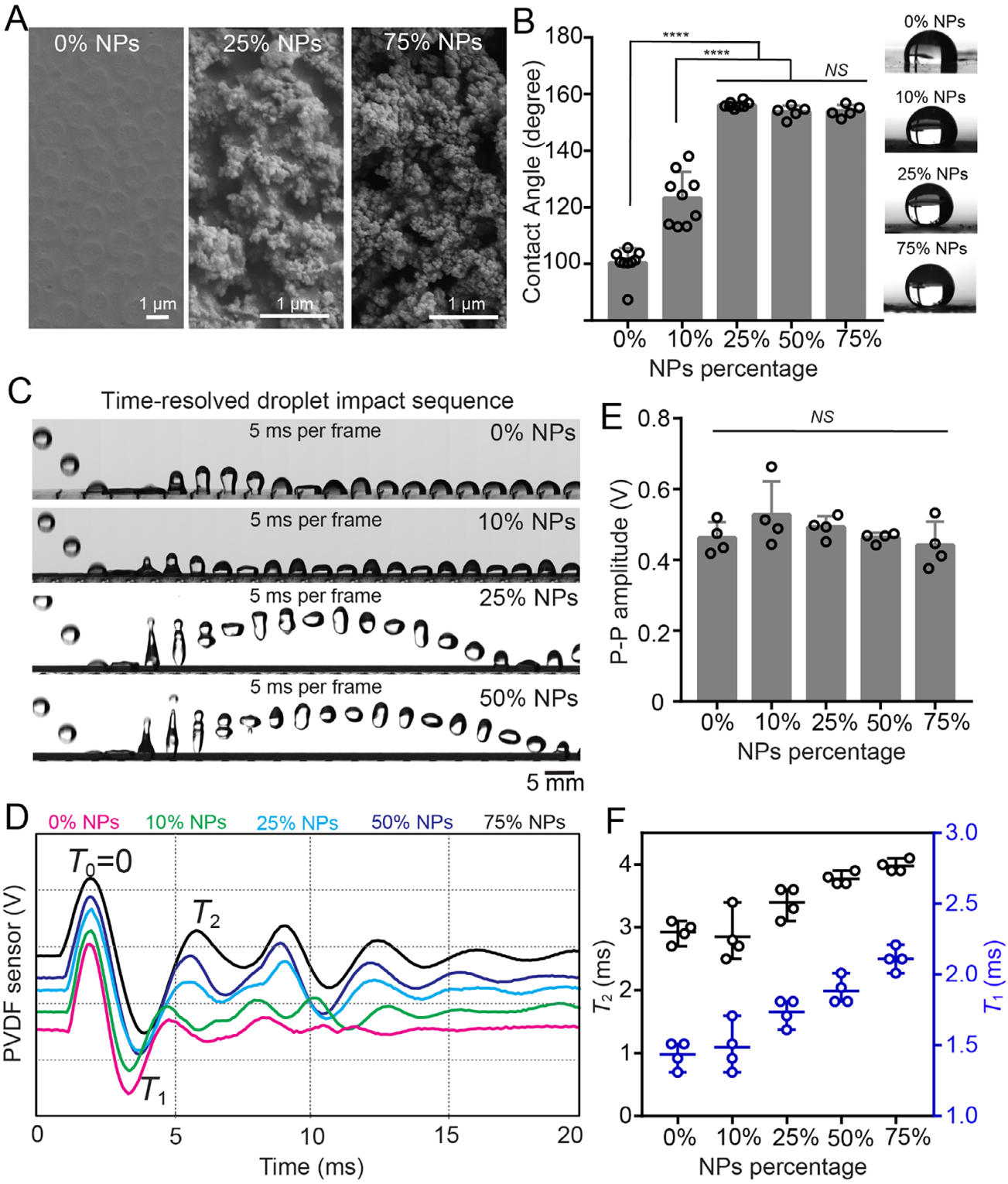

FIGURE 2 | Surface wettability and its effect on droplet impact dynamics. (A, B) SEM images (A) and quantitative analysis (B) of PS-coated glass substrates with different PFOTS-modified SiO_2 nanoparticle fractions. (C) High-speed images of droplet impact on high-adhesion and low-adhesion superhydrophobic substrates. (D) PVDF strain responses during the first 20 ms after impact. (E) Peak-to-peak PVDF strain amplitudes show no significant dependence on wettability. (F) Characteristic times T_1 and T_2 vary with nanoparticle fraction. Each data point represents an individual repeat experiment. NS, not significant; ****($p < 0.0001$).

16136829, 2026, 0, Downloaded from https://onlinelibrary.wiley.com/doi/10.1002/smll.74628. By Wiley Online Library, Wiley Online Library on [19/08/2026]. See the Terms and Conditions (https://onlinelibrary.wiley.com/terms-and-conditions) on Wiley Online Library for rules of use; OA articles are governed by the applicable Creative Commons License

We next focus on the first 20 ms following initial impact, before any rebound occurs. PVDF traces for substrates with different wettabilities reveal a robust pattern (Figure 2D). We define the first positive PVDF peak as $T_0 = 0$ ms, the subsequent negative peak as T_1, and the next positive peak as T_2. Here, T_1 captures the initial post-impact reversal, while T_2 defines the characteristic timescale of the first oscillation cycle. The peak-to-peak strain amplitude (P–P amplitude) varies only weakly across wettability (Figure 2E). In contrast, both T_1 and T_2 increase systematically with hydrophobicity, from 1.43 ± 0.10 to 2.10 ± 0.08 ms for T_1 and from 2.95 ± 0.17 to 3.98 ± 0.10 ms for T_2, as the contact angle increases from 100.4° (0% NPs) to 154.0° (75% NPs) (Figure 2F).

This behavior can be rationalized by treating the PVDF sensor output as a relative measure of substrate-coupled dynamic strain under fixed sensor geometry and amplifier conditions. During the earliest stage of impact [5, 6, 32], the characteristic inertial loading exerted by the droplet scales as $F_{\text{inertial}} \sim \rho V_0^2 D_0^2$, where ρ is the liquid density, V_0 the impact velocity, and D_0 the droplet diameter [23, 25, 26]. If the effective contact stiffness of the sensor-substrate system is k_c and the characteristic strained length is L_{eff}, the impact-induced displacement scales as $x \sim F_{\text{inertial}}/k_c$, and the corresponding substrate strain scales as $\varepsilon \sim x/L_{\text{eff}}$. Therefore, the peak-to-peak dynamic strain is associated with the first impact response $\varepsilon_{\text{pp}} \sim \rho V_0^2 D_0^2/(k_c L_{\text{eff}})$. Since k_c is dominated by substrate elasticity and depends only weakly on surface wettability over these sub-millisecond inertial timescales, the impulsive strain amplitude, and hence the first PVDF sensor's signal voltage peak, is essentially independent of contact angle. Under the same droplet size and release height, the initial momentum transfer to the substrate is similar across surfaces (Figure 2E).

In contrast, the timing parameters T_1 and T_2 reflect the post-impulse dynamics of the local liquid–solid interface [6, 21–23, 32]. In a simplified per-area description, the interfacial region can be treated as an effective mass m'_{eff} coupled to an effective stiffness, $k'_{\text{eff}}(\theta) = k'_c(\theta) + k'_\gamma(\theta)$, where $k'_c(\theta)$ represents contact-mediated stiffness and $k'_\gamma(\theta)$ represents capillary restoring stiffness. As the contact angle decreases, increased liquid–solid contact area, stronger contact-line constraint, and enhanced capillary coupling are expected to increase the effective interfacial stiffness. The characteristic oscillation period, therefore, scales as $T_2 \sim 2\pi\sqrt{\frac{m'_{\text{eff}}}{k'_{\text{eff}}(\theta)}}$. Accordingly, increasing $k'_{\text{eff}}(\theta)$ shortens the oscillation period T_2, and the first-lobe time T_1 follows the same decreasing trend. Thus, lowering the contact angle reduces both T_1 and T_2 (Figure 2F), consistent with enhanced effective interfacial stiffness and stronger liquid–solid coupling.

2.3 | Weber Number and Inertial Impact Time Govern the Amplitude and Timing of Early PVDF Responses

We next examined the dependence of the PVDF sensor-detected signal waveform on droplet diameter D_0 and impact height h on a fixed superhydrophobic substrate. The impact velocity, V_0, was calculated from the release height as $V_0 = \sqrt{2gh}$, and the corresponding Weber number was defined as $We = \rho V_0^2 D_0/\gamma$. Consistent with this inertial scaling, normalizing the P–P PVDF amplitude by droplet diameter, V_{PP}/D_0, increases approximately linearly with We (Figure 3A). These trends can be understood from the inertial loading scale during the earliest stage of impact [23, 26]. The characteristic normal loading scales as $F_{\text{inertial}} \sim \rho V_0^2 D_0^2$. Using $We = \rho V_0^2 D_0/\gamma$ this expression can be rewritten as $F_{\text{inertial}} \sim \gamma D_0 We$. Because the PVDF voltage is used here as a relative measure of substrate-coupled dynamic strain under a fixed sensor geometry and amplifier configuration, the first P–P voltage amplitude (V_{PP}) is expected to follow the same inertial loading trend [33–35]. Therefore, V_{PP} scales with $D_0 We$, and the normalized response V_{PP}/D_0 scales approximately with We. Notably, impacts in the higher regime ($We > 120$, Figure S6), where splashing or secondary droplet breakup occurs, still follow the same overall trend, indicating that the first PVDF amplitude is primarily governed by the initial inertial loading rather than by later-stage droplet morphology.

The characteristic times T_1 and T_2 reflect early substrate-coupled waveform dynamics following the first impact-induced PVDF peak [6, 22, 36]. The first-lobe time T_1 correlates positively with the inertial impact time $\tau_\rho = D_0/V_0$ for both non-splashing and splashing impacts, indicating that this initial post-peak reversal is governed primarily by local impact-driven deformation and momentum transfer (Figure 3B). In contrast, T_2 reflects the first oscillatory recovery after the impulsive event and depends on the impact regime. For non-splashing impacts, T_2 correlates positively with the inertio-capillary time $\tau_\gamma = (\rho D_0^3/\gamma)^{1/2}$, suggesting capillary-mediated recovery of a coherent droplet–substrate interfacial region (Figure 3C). For splashing impacts at higher Weber numbers, T_2 becomes nearly insensitive to droplet diameter, suggesting that breakup interrupts the global droplet-scale recovery and confines the measured response to a localized substrate-coupled oscillation.

3 | Discussion

A high temporal resolution PVDF strain sensor reveals a two-stage substrate-coupled mechanical response when water droplets impact solid surfaces at the initial contact stage. Across a broad range of wettability, droplet sizes, and impact velocities, each impact consists of an intense impulsive PVDF sensor's response followed by coherent interfacial oscillations whose timing is governed by an effective inertial capillary stiffness. The impulsive component is controlled by droplet inertia, as shown by the increase in diameter-normalized P–P amplitude with Weber number, while surface wettability and interfacial structure tune the oscillation period and damping. On a fixed superhydrophobic substrate, T_1 remains closely associated with the inertial impact time τ_ρ, consistent with an initial post-peak reversal governed by impact-driven deformation and momentum transfer. In contrast, T_2 reflects regime-dependent interfacial recovery: coherent non-splashing impacts retain inertio-capillary behavior, whereas splashing disrupts droplet-scale recovery and localizes the measured response [37]. A minimal reduced-order model provides a physical mapping between the PVDF sensor-detected signal waveform and the underlying early impact dynamics.

These mechanical signatures may also have broader implications for damage initiation and fatigue under repeated droplet

16136829, 2026, 0, Downloaded from https://onlinelibrary.wiley.com/doi/10.1002/smll.74628. By Wiley Online Library, Wiley Online Library on [19/08/2026]. See the Terms and Conditions (https://onlinelibrary.wiley.com/terms-and-conditions) on Wiley Online Library for rules of use; OA articles are governed by the applicable Creative Commons License

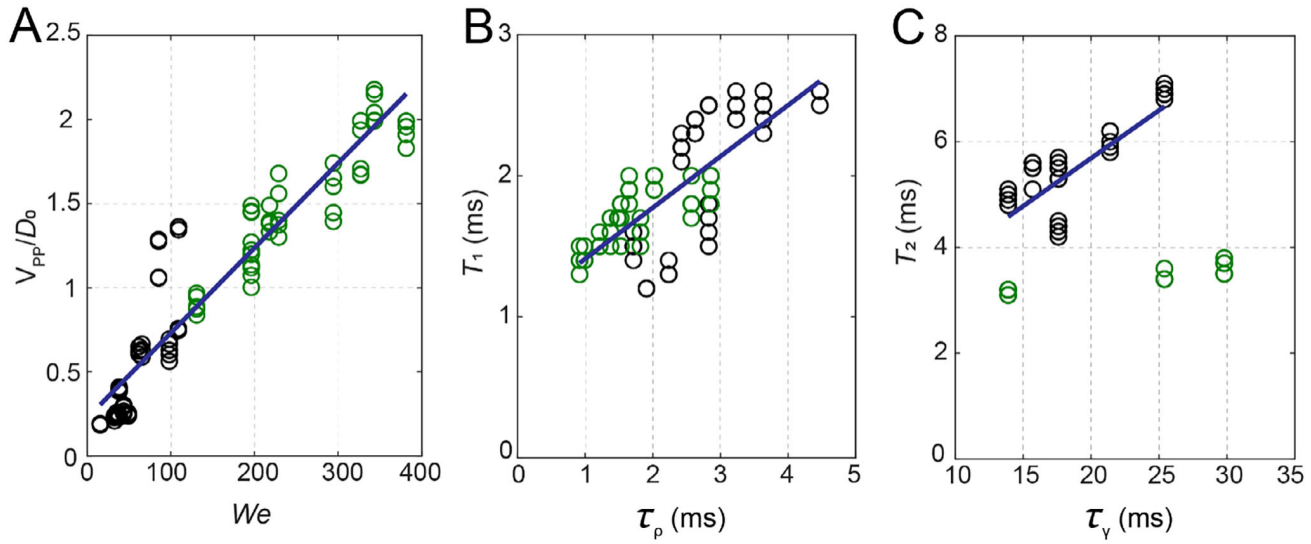

FIGURE 3 | Weber-number and characteristic-timescale dependence of early PVDF responses. (A) Diameter-normalized peak-to-peak PVDF amplitude, V_{PP}/D_0, plotted as a function of Weber number, $We = \rho V_0^2 D_0/\gamma$, on a fixed superhydrophobic substrate. (B) First-lobe time T_1 plotted against the inertial impact time $\tau_\rho = D_0/V_0$. (C) Oscillation period T_2 plotted against the inertio-capillary time $\tau_\gamma = (\rho D_0^3/\gamma)^{1/2}$. Black dots denote low-*We* non-splashing impacts ($15 < We < 120$); green dots denote high-*We* splashing impacts ($120 < We < 400$). Each data point represents an individual repeat experiment.

impacts. The initial impulsive pulse acts as a localized, shock-like load that stresses the near-surface region on millisecond timescales, potentially approaching the dynamic strength limits of brittle materials. The subsequent oscillations occur at frequencies comparable to the natural resonance band of many rocks, concretes, and engineered ceramics, typically in the range of 100–500 Hz. Repeated impacts could therefore activate a coupled mechanism in which the impulsive loading seeds microcracks, while the oscillatory interfacial forcing drives their growth through fatigue and resonant coupling. These findings suggest that the combined impulsive and oscillatory responses may contribute to progressive material weakening during rainfall-induced weathering and other droplet-driven erosion processes [1, 2]. In addition, the modulation of early-stage oscillation dynamics by surface wettability indicates that superhydrophobic modification can alter these oscillations and may help protect surfaces from impact-induced erosion and fracture.

Several limitations should be noted. First, the PVDF sensor's output reports a relative dynamic loading response rather than a static force. Because piezoelectric signals are sensitive to time-dependent deformation and can be affected by charge leakage and circuit-dependent decay, the measured waveform should be interpreted under the fixed sensor geometry and amplifier configuration used here. Absolute force quantification would require independent dynamic calibration of the complete sensor–circuit system. Second, this study focuses on water droplets in low- to moderate-speed impact regimes. For more viscous liquids, viscous dissipation may damp or shift the early interfacial oscillations. At higher Weber numbers, splashing, compressibility, water-hammer pressure, and cavitation may become increasingly important and may alter the measured waveform. Future work will extend this measurement approach across broader Weber-number, Reynolds-number, and Ohnesorge-number regimes to capture transitions among inertial, capillary, viscous, and compressible impact dynamics.

4 | Conclusion

In summary, a high-temporal-resolution PVDF strain sensor reveals a two-stage substrate-coupled mechanical response during the initial contact stage of water-droplet impact on solid surfaces. Across a broad range of wettability, droplet sizes, and impact velocities, each impact produces an intense impulsive PVDF response followed by coherent interfacial oscillations. The impulsive component is governed by droplet inertia, as shown by the increase in diameter-normalized P–P amplitude with Weber number, while the early waveform features arise from impact-driven deformation and momentum transfer. The subsequent oscillations reflect substrate-coupled deformation–recovery dynamics at the water–solid interface, with surface wettability, interfacial structure, and impact regime modulating the oscillation period and damping. These measurements and the reduced-order model provide a physical framework for mapping PVDF waveforms to early droplet-impact dynamics.

Author Contributions

Ian Kim, Siyuan Rao, and Qianbin Wang conceptualized the idea and designed all the experiments. Ian Kim, Chen Lin, and Zuer Wu led the main experiments and data analysis. All authors worked on the interpretation of the data and contributed to writing the manuscript.

Acknowledgements

This study was supported by Binghamton University faculty start-up funding (Siyuan Rao and Qianbin Wang) and by the National Science Foundation CAREER Program (2414753 to Siyuan Rao; 2442112 to Qianbin

16136829, 2026, 0, Downloaded from https://onlinelibrary.wiley.com/doi/10.1002/smll.74628. By Wiley Online Library, Wiley Online Library on [19/08/2026]. See the Terms and Conditions (https://onlinelibrary.wiley.com/terms-and-conditions) on Wiley Online Library for rules of use; OA articles are governed by the applicable Creative Commons License

Wang), S.H. Ho Foundation Research Grants for Health Sciences and Technology, Binghamton University Watson College of Engineering and Applied Science Seed Grant Program (105383), Binghamton University Transdisciplinary Areas of Excellence (TAE) program, and the Binghamton University S3IP Small Grant award (ADLG267 and 324 to Siyuan Rao; ADLG274 to Qianbin Wang). We also acknowledge the essential resources provided by the Binghamton University core facilities, particularly the Electron Microscopy Suite within the Materials Science Core Facility at the Analytical and Diagnostics Laboratory (ADL).

Conflicts of Interest

The authors declare no conflicts of interest.

Data Availability Statement

The data that support the findings of this study are available from the corresponding author upon reasonable request.

References

1. M. Elhadi Ibrahim and M. Medraj, "Water Droplet Erosion of Wind Turbine Blades: Mechanics, Testing, Modeling and Future Perspectives," *Materials* 13, no. 1 (2019): 157.

2. M. Marzbali, F. Yeganehdoust, M. E. Ibrahim, F. Tarasi, and M. Jadidi, "Liquid-Solid Impact Mechanism, Liquid Impingement Erosion, and Erosion-Resistant Surface Engineering: A Review," *Coatings* 13, no. 3 (2023): 577.

3. P. Kinnell, "Raindrop-Impact-Induced Erosion Processes and Prediction: A Review," *Hydrological Processes* 19, no. 14 (2005): 2815–2844.

4. T. P. Sun, F. Álvarez-Novoa, K. Andrade, P. Gutiérrez, L. Gordillo, and X. Cheng, "Stress Distribution and Surface Shock Wave of Drop Impact," *Nature Communications* 13, no. 1 (2022): 1703.

5. A. L. Yarin, "Drop Impact Dynamics: Splashing, Spreading, Receding, Bouncing…," *Annual Review of Fluid Mechanics* 38, no. 1 (2006): 159–192.

6. X. Cheng, T. P. Sun, and L. Gordillo, "Drop Impact Dynamics: Impact Force and Stress Distributions," *Annual Review of Fluid Mechanics* 54, no. 1 (2022): 57–81.

7. M. Rein, "Phenomena of Liquid Drop Impact on Solid and Liquid Surfaces," *Fluid Dynamics Research* 12, no. 2 (1993): 61–93.

8. D. Quéré, "Non-Sticking Drops," *Reports on Progress in Physics* 68, no. 11 (2005): 2495.

9. Z. Zhao, W. Li, X. Hu, et al., "The Limit of Droplet Rebound Angle," *Nature Communications* 16 (2025): 5684.

10. Z. Hu, H. Ran, H. Shan, F. Chu, Z. Wang, and R. Wang, "Reconsideration on the Maximum Deformation of Droplets Impacting on Solid Surfaces," *Droplet* 4, no. 2 (2025): 163.

11. F. Yu, A. D. Ratschow, R. Tao, et al., "Why Charged Drops Do Not Splash," *Physical Review Letters* 134, no. 13 (2025): 134001.

12. Y. Liu, L. Moevius, X. Xu, T. Qian, J. M. Yeomans, and Z. Wang, "Pancake Bouncing on Superhydrophobic Surfaces," *Nature Physics* 10, no. 7 (2014): 515–519.

13. Y. Li, W. Zhao, Y. Zhou, et al., "Ultrafast Bounce of Particle-Laden Droplets," *Nature Communications* 15, no. 1 (2024): 9943.

14. H. Y. Kim, S. Y. Park, and K. Min, "Imaging the High-Speed Impact of Microdrop on Solid Surface," *Review of Scientific Instruments* 74, no. 11 (2003): 4930–4937.

15. J. Zaal, W. D. van Driel, F. J. H. G. Kessels, and G. Q. Zhang, "Correlating Drop Impact Simulations With Drop Impact Testing Using High-Speed Camera Measurements," *Journal of Electronic Packaging* 131, no. 1 (2009): 011007.

16. B. Zhang, V. Sanjay, S. Shi, et al., "Impact Forces of Water Drops Falling on Superhydrophobic Surfaces," *Physical Review Letters* 129, no. 10 (2022): 104501.

17. J. Li, A. Oron, and Y. Jiang, "Droplet Jump-Off Force on a Superhydrophobic Surface," *Physical Review Fluids* 8, no. 11 (2023): 113601.

18. Z. Hu, F. Chu, and X. Wu, "Double-Peak Characteristic of Droplet Impact Force on Superhydrophobic Surfaces," *Extreme Mechanics Letters* 52 (2022): 101665.

19. C. Antonini, F. Villa, I. Bernagozzi, A. Amirfazli, and M. Marengo, "Drop Rebound After Impact: The Role of the Receding Contact Angle," *Langmuir* 29, no. 52 (2013): 16045–16050.

20. D. Richard, C. Clanet, and D. Quéré, "Contact Time of a Bouncing Drop," *Nature* 417, no. 6891 (2002): 811–811.

21. L. Rayleigh, "On the Capillary Phenomena of Jets," *Proceedings of the Royal Society of London* 29 (1879), 71–97.

22. A. Prosperetti, "Free Oscillations of Drops and Bubbles: The Initial-Value Problem," *Journal of Fluid Mechanics* 100, no. 2 (1980): 333–347.

23. L. Duchemin and C. Josserand, "Curvature Singularity and Film-Skating During Drop Impact," *Physics of Fluids* 23, no. 9 (2011): 091701.

24. Y. Zhou, C. Zhang, W. Zhao, S. Wang, and P. Zhu, "Suppression of Hollow Droplet Rebound on Super-Repellent Surfaces," *Nature Communications* 14, no. 1 (2023): 5386.

25. B. R. Mitchell, J. C. Klewicki, Y. P. Korkolis, and B. L. Kinsey, "The Transient Force Profile of Low-Speed Droplet Impact: Measurements and Model," *Journal of Fluid Mechanics* 867 (2019): 300–322.

26. V. Sanjay and D. Lohse, "Unifying Theory of Scaling in Drop Impact: Forces and Maximum Spreading Diameter," *Physical Review Letters* 134, no. 10 (2025): 104003.

27. C. A. Banciu, E. Chitanu, T. Mălăeru, et al., "Comparative Study of the Hydrophobic Properties of Silicon Dioxide Particles Functionalized With Different Agents," *Journal of Optoelectronics and Advanced Materials* 25, no. 1-2 (2023): 89–95.

28. B. Su, Y. Tian, and L. Jiang, "Bioinspired Interfaces With Superwettability: From Materials to Chemistry," *Journal of the American Chemical Society* 138, no. 6 (2016): 1727–1748.

29. S. Wang, K. Liu, X. Yao, and L. Jiang, "Bioinspired Surfaces With Superwettability: New Insight On Theory, Design, and Applications," *Chemical Reviews* 115, no. 16 (2015): 8230–8293.

30. D. Richard and D. Quéré, "Bouncing Water Drops," *Europhysics Letters* 50, no. 6 (2000): 769.

31. J. C. Bird, R. Dhuman, H. M. Kwon, and K. K. Varanasi, "Reducing the Contact Time of a Bouncing Drop," *Nature* 503, no. 7476 (2013): 385–388.

32. C. Josserand and S. T. Thoroddsen, "Drop Impact on a Solid Surface," *Annual Review of Fluid Mechanics* 48, no. 1 (2016): 365–391.

33. A. S. Grinspan and R. Gnanamoorthy, "Impact Force of Low Velocity Liquid Droplets Measured Using Piezoelectric PVDF Film," *Colloids and Surfaces A: Physicochemical and Engineering Aspects* 356, no. 1-3 (2010): 162–168.

34. A. Imeson, R. Vis, and E. De Water, "The Measurement of Water-Drop Impact Forces With a Piezo-Electric Transducer," *Catena* 8, no. 1 (1981): 83–96.

35. C. V. Dung and E. Sasaki, "Numerical Simulation of Output Response of PVDF Sensor Attached on a Cantilever Beam Subjected to Impact Loading," *Sensors* 16, no. 5 (2016): 601.

36. C. Clanet, C. Béguin, D. Richard, and D. Quéré, "Maximal Deformation of an Impacting Drop," *Journal of Fluid Mechanics* 517 (2004): 199–208.

37. T. Kondo and K. Ando, "Simulation of High-Speed Droplet Impact Against a Dry/Wet Rigid Wall for Understanding the Mechanism of Liquid Jet Cleaning," *Physics of Fluids* 31, no. 1 (2019): 013303.

16136829, 2026, 0, Downloaded from https://onlinelibrary.wiley.com/doi/10.1002/smll.74628. By Wiley Online Library, Wiley Online Library on [19/08/2026]. See the Terms and Conditions (https://onlinelibrary.wiley.com/terms-and-conditions) on Wiley Online Library for rules of use; OA articles are governed by the applicable Creative Commons License

Supporting Information

Additional supporting information can be found online in the Supporting Information section.

Supporting File: smll74628-sup-0001-SuppMat.docx.

16136829, 2026, 0, Downloaded from https://onlinelibrary.wiley.com/doi/10.1002/smll.74628. By Wiley Online Library, Wiley Online Library on [19/08/2026]. See the Terms and Conditions (https://onlinelibrary.wiley.com/terms-and-conditions) on Wiley Online Library for rules of use; OA articles are governed by the applicable Creative Commons License